AIAA 81-4168

Control Law Synthesis for Flutter Suppression Using Linear Quadratic Gaussian Theory

J.K. Mahesh* and C.R. Stone†
Honeywell Systems and Research Center, Minneapolis, Minn.
W.L. Garrard‡
University of Minnesota, Minneapolis, Minn.
and
H.J. Dunn§
NASA Langley Research Center, Hampton, Va.

This paper describes the application of linear quadratic Gaussian (LQG) methodology to the design of active control systems for suppression of aerodynamic flutter. A wind tunnel model of a research wing with associated sensors and actuators comprises the system to be controlled. Results of a synthesis methodology that provide small values of rms response and robust stability are presented. Results of control surface and sensor position optimization are also presented. Both frequency response matching and modal residualization are used to obtain practical flutter controllers.

Nomenclature

Scalars

b	= design parameter for robust Kalman estimator
c	= reference chord length
$E\{\ \}$	= expected value operator
$h(x,y,t)$	= deflection of wing at point (x,y) and time t
J	= performance index
k	= reduced circular frequency $= \omega c/2V$
$\hat{k}_m$	= reduced frequency used in modeling unsteady aerodynamic forces
l	= reference length for wind gust model
M	= Mach number
q_i	= generalized coordinate representing ith flexure mode
$\bar{q}$	= dynamic pressure $= \frac{1}{2}\rho V^2$
s	= Laplace operator
t	= time
u	= actuator input
V	= freestream velocity
w	= vertical wind gust velocity
x,y	= spatial coordinates of wing
$Z_i(x,y)$	= displacement influence coefficient associated with flexure coordinate q_i
δ	= control surface displacement
η_1	= white noise forcing function for wind gust model
η_2	= white noise forcing function for sensor noise
ρ	= air density
σ	= rms wind gust velocity
ω	= circular frequency

Vectors

g_i	= see Eq. (5a)
m	= measured acceleration vector
q	= vector of generalized flexure coordinates
Z_s	= vector of displacement influence coefficients evaluated at point (x_s,y_s)
x	= state vector
x_1	$= q$
x_2	$= \dot{q}$
$x_3 \ldots x_{2+L}$	= aerodynamic lag states

Matrices

A_i, D_i	= real aerodynamic matrices
C	= see Eq. (5b)
F	= see Eq. (5a)
K	= generalized stiffness matrix
M	= generalized mass matrix
Q	= matrix of unsteady aerodynamic force coefficients
R	= control weighting matrix
S	= state weighting matrix
Z	= matrix of displacement influence coefficients

Submitted Jan. 25, 1980; revision received Aug. 11, 1980.

*Senior Research Engineer.
†Staff Engineer. Associate Fellow AIAA.
‡Associate Professor, Department of Aerospace Engineering and Mechanics. Member AIAA.
§Aerospace Engineer.

I. Introduction

ENERGY-efficient air transports of the future may require active systems for flutter suppression to realize full benefits of proposed improvements in wing design. Application of active flutter suppression can result in substantial weight savings and increased performance compared with passive methods such as increased structural stiffness, mass balancing, and speed restrictions.[1] The objective of this paper is to demonstrate the application of an active flutter control design methodology based on Linear Quadratic Gaussian (LQG) theory to the design of flutter-suppression system for a wind tunnel model of the DAST (Drones for Aerodynamic and Structural Testing) wing.[2] The DAST wing is a supercritical design aerodynamically and structurally similar to those proposed for future air transports, and will, if uncontrolled, flutter within the flight envelope of the DAST vehicle (a Firebee II Drone).

Several techniques have been used to design flutter control systems for the DAST wing. Abel et al.[3] compare two flutter control systems. One system design is based on classical feedback control techniques[4] and the other on the aerodynamic energy method of Nissim.[5] Both systems achieve the objective of 44% increase in flutter dynamic pressure but the aerodynamic energy method results in lower levels of control surface activity than classical techniques. Newsom[6] applies linear quadratic optimal control theory to flutter suppression of a wind tunnel model of the DAST wing

and Abel et al.[7] describe an analytical and experimental comparison of the resulting controller with a controller designed using the aerodynamic energy approach.

In this paper, two methods are used to design full-state feedback flutter controllers for the wind tunnel model of the DAST wing. Control surface location is optimized by T.L. Johnson's method.[8] Initial sensor location is obtained by observability considerations and the Doyle and Stein procedure[9] is used to design robust Kalman estimators which exhibit improved stability margins compared with conventional Kalman estimators. Sensor locations are optimized for the robust Kalman estimator designs for single and double sensor complements. The resulting robust controllers are practicalized by residualization and frequency response matching techniques. The performance of the residualized single-sensor controller is evaluated over a range of dynamic pressures and Mach numbers and is shown to compare favorably in terms of rms response and stability margins with designs based on the aerodynamic energy approach and linear optimal control theory.[7]

II. Modeling

The system to be controlled consists of a wing, a control surface, an actuator, and a set of accelerometers used to sense the motion of the wing. The geometry of the wing and candidate accelerometer locations are shown in Fig. 1. The elastic deformation of the wing is approximated by a finite, linear combination of the normal modes of vibration:

$$h(x,y,t) \cong \sum_{i=1}^{n} Z_i(x,y)\,q_i(t) \tag{1}$$

The elastic influence coefficients and generalized mass and stiffness matrices corresponding to the first ten modes are calculated using a NASTRAN finite-element model of the wing. The equations of motion for the flexure coordinates are written in vector-matrix form as

$$[Ms^2+K]q = -\bar{q}Q(s,\bar{M})\begin{pmatrix} q \\ \delta \\ w \end{pmatrix} \tag{2}$$

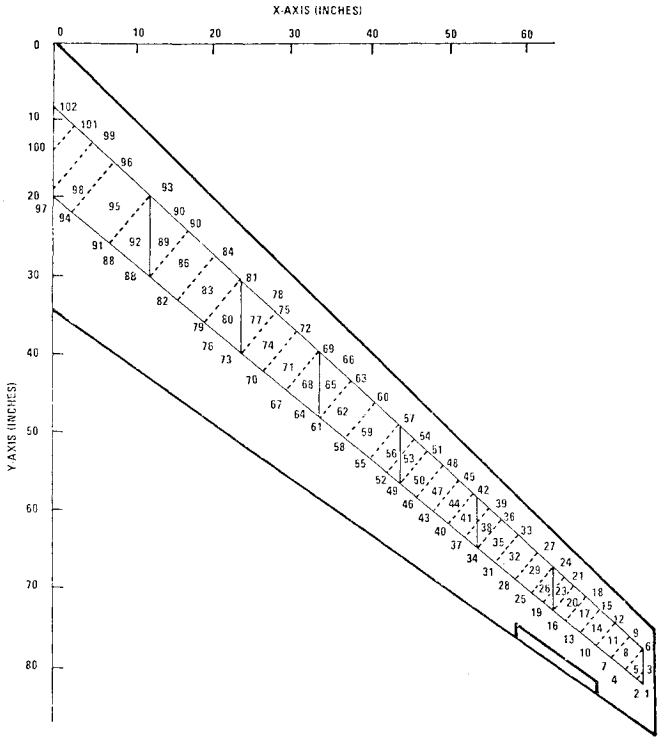

Fig. 1 DAST wind tunnel model.

(Structural damping is not included in the above equation.) The right side of Eq. (2) represents the vector of unsteady aerodynamic forces expressed as a linear combination of the flexure modes, control surface deflection, and vertical wind gust velocity. Assuming steady-state oscillatory motion of the wing, the elements of the Q matrix are calculated numerically using the doublet lattice method[10] for three Mach numbers (0.7, 0.8, 0.9) and eight reduced frequencies ranging from 0 to 1.2. This results in a complex Q matrix which is approximated for nonoscillatory motion by a rational matrix polynomial in s of the form

$$Q(s,\bar{M}) \cong A_0 + A_1\left(\frac{cs}{2V}\right) + A_2\left(\frac{cs}{2V}\right)^2 + \sum_{m=1}^{L} \frac{D_m s}{s+(2V/c)\hat{k}_m} \tag{3}$$

The form of this approximation was suggested by Sevart[11] and appears to be based on the work of R.T. Jones.[12] Other approaches to modeling the unsteady aerodynamics have been proposed[13-15]; however, the approximation given by Eq. (3) has been successfully used by other researchers in designing flutter controllers for the DAST wing.[3-7] The values of $\hat{k}_m$ are selected from the reduced frequencies for which $Q(jk,\bar{M})$ has been calculated. Only a few values of $\hat{k}_m$ near the reduced flutter frequency are required. The A and D matrices in Eq. (3) are constrained to be real and are computed at each Mach number to give the best least-squares fit to $Q(jk,\bar{M})$ over the range of reduced frequencies from 0 to 1.2.

Combining Eqs. (2) and (3) yields the equations of motion in vector-matrix form as

$$[Ms^2+K]q + \bar{q}\left[A_0 + A_1\left(\frac{cs}{2V}\right) + A_2\left(\frac{cs}{2V}\right)^2 + \sum_{m=1}^{L} \frac{D_m s}{s+(2V/c)\hat{k}_m}\right]\begin{bmatrix} q \\ \delta \\ w \end{bmatrix} = 0 \tag{4}$$

The measured acceleration vector is modeled as a linear combination of the actual acceleration and sensor noise. The sensor for each accelerometer is assumed to be identical and based on previous experience, and is approximated by white noise with intensity 6.45×10^{-4} m^2/s^4 (1 in.^{2}/s^4).

The equations of motion for the flutter system can be written as a set of first-order linear ordinary differential equations of the form

$$\dot{x} = Fx + g_1\delta + g_2 w \tag{5a}$$

$$m = Cx + \eta_2 \tag{5b}$$

Calculating the roots of Eq. (5a) as a function of dynamic pressure reveals (Fig. 2) that classical bending-torsion flutter occurs at a dynamic pressure of 4.96 kPa (103.6 psf) and a frequency of 8.029 Hz. This result compares favorably with experimentally determined values of 4.92 kPa (102.7 psf) and 7.7 Hz.[7]

An electrohydraulic servo-actuator is used to drive the control surface. The transfer function of this actuator was experimentally measured[16] and is approximated by

$$\frac{\delta}{u} = \frac{214\times89{,}450}{(s+214)(s^2+179.4s+89{,}450)} \tag{6}$$

First- and second-order Dryden models are used for the vertical wind gust. The transfer function for the first-order Dryden model is

$$\frac{w(s)}{\eta_1(s)} = \frac{\sigma\sqrt{v/l}}{s+\sqrt{v/l}} \tag{7a}$$

and the transfer function of the second-order Dryden model is

$$\frac{w(s)}{\eta_1(s)} = \frac{\sigma\sqrt{l/v}\,(1+\sqrt{3l/v}\,s)}{[1+(l/v)s]^2} \tag{7b}$$

The design model includes five flexure modes, five first-order unsteady aerodynamic states, a third-order actuator model and either a first-or second-order Dryden wind model with l equal to 30.48 m (100 ft).

III. Full-State Feedback Design

The performance objective is to stabilize the wing at a design condition of Mach number 0.9 and a dynamic pressure of 7.66 kPa. The final controller should have rms response values for aileron deflection and deflection rate of less than 4 deg and 250 deg/s for an rms wind gust of 0.3048 m/s (1 ft/s). Gain margins should be 6 dB or greater and phase margins should be 60 deg or greater.

Design with Prescribed Control Surface

A full-state feedback controller is designed using linear optimal control theory.[17] This controller should result in rms control surface activity about 35% smaller than the final allowable values to allow for performance deterioration at subsequent design steps. The full-state feedback gains minimize the quadratic performance index.

$$J=\mathrm{E}\{x^T Sx+u^T Ru\} \tag{8}$$

Two methods are used to select the quadratic weights in Eq. (8). The baseline method is an iterative procedure in which the designer varies the weights until the resulting controller meets the performance specifications. The second method is an asymptotic procedure due to Sirisena[18] in which the quadratic weights are selected to achieve prescribed closed-loop poles.

The results of both quadratic weight selection procedures are summarized in Table 1. Columns S and 1 present results with the first order wind model. Both the Sirisena (S) and the baseline method (1) result in acceptable rms responses. The Sirisena design is slightly better; however, since the Sirisena method is computationally more complicated, the remaining designs are accomplished using the baseline method. Columns 2-4 present results with the second-order wind model. Cases 1 and 2 use the same quadratic weights. The rms responses are 40% greater with the second-order wind model. For case 3 only the control is weighted. This control reflects the unstable poles about the imaginary axis and does not affect the other poles.[17] For cases 2 and 3 there are no weights on δ or $\dot{\delta}$. Actuator poles are near their open-loop values but rms response values are too close to their limit values; therefore, δ and/or $\dot{\delta}$ are weighted to reduce rms control responses. Case 4 gives acceptable rms responses and defines the full-state feedback control which forms the basis for the remainder of the design.

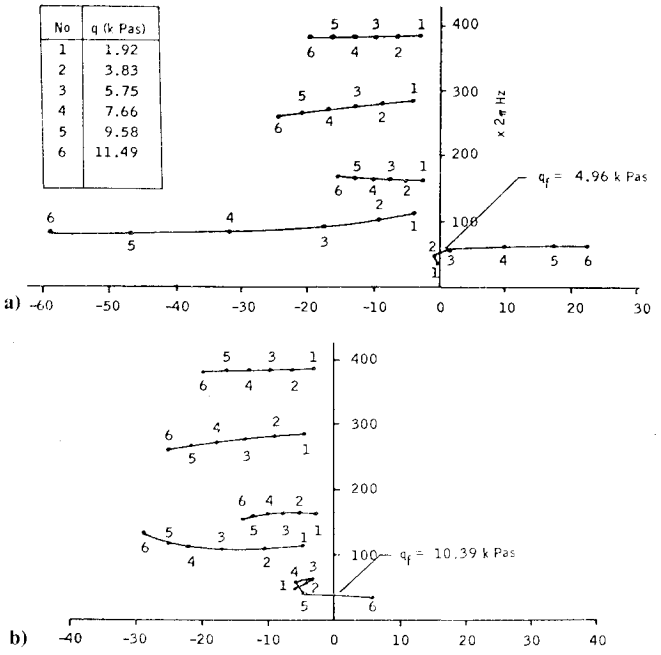

Fig. 2 Root locus at $M=0.9$; a) open-loop; b) with flutter suppression control.

Control Surface Optimization

The results described above are obtained with the nominal control surface location shown in Fig. 1. A method due to Johnson[8] is used to optimize control surface placement. The value of the performance index J [Eq. (8)] is a function of the control surface locations as well as the state feedback gains. Johnson's method uses a gradient procedure to calculate the value of the control surface location which minimizes J. The optimal state feedback gains for the particular control surface location are used at each gradient iteration step. The details of the application of this method are described in Ref. 19 and the results are summarized in Table 2.

Row 1 entry is with the nominal control surface location but employs a polynomial fit model for the aileron

Table 1 Full-state feedback controller synthesis summary

Case	S	1	2	3	4
Quadratic weights on indicated variables:					
$\dot{q}_1$		s	s	0	s
$\dot{q}_2$		s	s	0	s
$\dot{q}_3$		s	s	0	s
$\dot{q}_4$		s	s	0	s
$\dot{q}_5$		s	s	0	s
δ		0	0	0	0
$\dot{\delta}$		0	0	0	2
u		50,000	50,000	50,000	50,000
Rms response:					
δ	1.788	1.804	2.548	2.492	2.579
$\dot{\delta}$	151.4	164.9	229.5	218.0	189.4
Quadratic cost × 10:					
J		0.02384	0.4702	0.3210	0.5529
Actuator poles:					
Real	−221.5	−212.5	−212.5	−214.8	−138.6
Freq.	47.60	47.76	47.76	47.60	58.57
Damping factor	0.3000	0.2994	0.2994	0.2994	0.5260

s is the quadratic weight placed on the modal velocities. The modal displacements, unsteady aerodynamic states, and vertical wind gust states are unweighted.

Table 2 Control surface position optimization

Aileron position		Rms						
Inboard semispan	Outboard semispan	δ, deg	$\dot{\delta}$, deg/s	J	DJ_{ij}	i	j	No.
.763	.893	2.594	190.5	.5576E 06	...	...	...	1
.753	.883	2.620	192.0	.5668E 06	.9047E 04	1	2	2
.783	.913	2.584	188.5	.5438E 06	−.1434E 05	1	3	3
.807	.937	2.510	187.2	.5338E 06	−.2582E 05	1	4	4
.730	.937	1.717	124.2	.2981E 06	.5753E 05	6	5	5
.660	.937	1.428	97.7	.2308E 06	−.8458E 06	5	6	6

Table 3 Robustness summary

			Rms		Gain margin				Phase margin				Bandwidth,
Control	Sensor	b	δ, deg	$\dot{\delta}$, deg/s	dB	Hz	dB	Hz	deg	Hz	deg	Hz	Hz
State	State	0.0	1.804	164.9	−8.1	9.90	∞	...	−63.7	7.05	+82.3	15.25	23.2
Kalman	16,57	0.0	2.330	186.2	−5.3	10.28	+6.4	21.87	−42.5	8.26	+32.4	13.64	59.8
Robust	16,57	0.000001	2.733	196.8	−6.6	9.85	20.0	75.28	−45.4	7.46	+66.2	13.56	19.3
Robust	16,57	0.00001	3.066	212.0	−7.3	9.87	21.5	103.56	−53.3	7.23	+72.9	14.23	11.1
Robust	16,57	0.0001	3.534	240.2	−7.7	9.90	24.9	149.65	−57.9	7.16	+76.3	14.64	21.8
Kalman	18	0.0	2.383	197.9	−3.9	10.49	+3.0	17.1	−43.9	8.71	+18.3	13.15	44.9
Robust	18	0.000001	4.018	158.5	−4.5	9.82	+8.4	4.84	−29.1	7.97	+43.9	12.21	15.3
Robust	18	0.00001	6.445	197.4	−5.6	9.72	+7.7	3.95	−34.3	7.48	+58.2	12.62	16.6
Robust	18	0.0001	11.534	243.4	−6.3	9.74	+7.9	3.01	−40.5	7.21	+65.6	13.10	17.8
Kalman	28	0.0	2.607	194.3	−1.8	61.20	+3.7	18.54	−41.5	8.55	+22.8	13.62	64.6
Robust	28	0.000001	3.781	164.6	−5.6	4.85	+26.3	2.21	−37.9	7.81	+55.6	12.75	16.7
Robust	28	0.00001	5.069	188.2	−6.8	9.80	+28.9	1.56	−46.2	7.31	+71.1	13.67	18.5
Robust	28	0.0001	6.998	204.7	−7.5	9.85	+50.7	0.37	−55.2	7.10	+76.6	14.42	21.2

aerodynamic data. Rows 1-4 establish that, for ailerons whose span is 13% of the wing semispan, the most outboard allowable position is best. In the first iteration (row 2) the aileron was moved inboard and δ, $\dot{\delta}$, and J all increase. The one-sided difference (DJ) used in the gradient procedure is an excellent approximation to the differences in values of J. This assures monotonicity for incremental inboard shifts in aileron of less than 1% of semispan and provides reasonable assurance that inboard shifts are undesirable.

The aileron is then moved outboard from its nominal position in two steps (rows 3 and 4) to its maximum allowable value. The values of δ, $\dot{\delta}$, and J are monotone decreasing and DJ's are again a good approximation to the changes in J. It is clear that the outboard aileron position is optimum among those whose span is 13% of the wing semispan, however, the improvements over the nominal position are less than 5%.

The previous results indicate the aileron should be as far outboard as possible. If further improvements are desirable it is necessary to increase the aileron span. The outboard position is held at its maximum value and the aileron span is increased by moving the aileron inboard position to the inboard extreme. This was done in two steps shown in rows 5 and 6. The values of δ, $\dot{\delta}$, and J are decreased by about 45%. Since the basic objective of this study is to design controllers which can be implemented on the existing wind tunnel model of the DAST wing, the nominal control surface defined in Fig. 1 is used for all subsequent design work.

IV. Kalman Estimator Design

Initial Sensor Placement

Three sets of sensor locations are selected initially. The first set consisting of two accelerometers is obtained by an adaption of a method due to R.G. Brown.[21] The sensor complement is considered a good choice if it spans the mode acceleration space well. The degree of spanning the mode acceleration space is determined by computing the minimum eigenvalue of ZZ^T matrix where Z is the mode acceleration coefficient matrix of the sensor complement. Accelerometers at node points 16 and 57 are best. The second and third sensor sets consist of single accelerometers placed on the leading edge (node position 18) and trailing edge (node position 28) of the wing spar.

Robust Design

As shown in Table 3 the full-state feedback system is unconditionally stable, has good gain and phase margins (robustness) and low bandwidth. If an ordinary Kalman estimator is used to estimate the states, the robustness properties are seriously degraded for all sensor complements (see Table 3). A design procedure due to Doyle and Stein[9] is used to improve the robustness of the Kalman estimator.

The robust Kalman estimator is obtained by adding a fictitious noise directly to the control input of the plant during the estimator design. This noise is characterized by a design parameter b proportional to the covariance of the added noise. For $b=0$, the ordinary Kalman estimator results. As b is increased the estimator becomes more robust; however, rms responses increase. If the sensor complement results in a minimum phase transfer function between the control input and sensor output, the stability characteristics are guaranteed to approach those of full-state feedback as b approaches infinity.[9] The results of the robust estimator design procedure are shown in Table 4 for the three sets of sensors described above. Accelerometers at points 16 and 28 result in minimum phase transfer functions while 57 and 18 result in nonminimum phase transfer functions.

Values for rms responses are presented in Table 4. Best response is obtained with full-state feedback. There are modest increases in rms response with the ordinary Kalman estimators. There are further increases in rms response with the robust Kalman estimators (modest for the minimum phase cases and severe for the nonminimum phase case). With full-state feedback, gain and phase margins are excellent and the bandwidth is low. With the ordinary Kalman estimator, gain and phase margins are relatively poor and the bandwidth is large. As robustness increases there is a monotone transition from the ordinary Kalman to full-state feedback stability. Robustness is more easily achieved with sensors which result

Table 4 Single sensor robust controller performance

Control	Sensor node position	Rms δ, deg	Rms $\dot{\delta}$, deg/s	Rms J, ($\times 10^7$)
State	...	2.579	189.4	.05529
Kalman	4 (2T)	3.333	186.6	.08565
Robust	16	4.047	218.7	.1385
Robust	19	4.156	223.7	.1484
Robust	22	4.201	225.1	.1444
Robust	19 (2T)	3.888	214.8	.1361
Robust	16 (2T)	3.788	207.8	.1302
Robust	13 (2T)	3.732	207.8	.1310
Robust	10 (2T)	3.683	207.0	.1295
Robust	7 (2T)	3.630	207.9	.1283
Robust	4 (2T)	3.595	209.7	.1277
Robust	4 (3T)	3.471	205.4	.1253

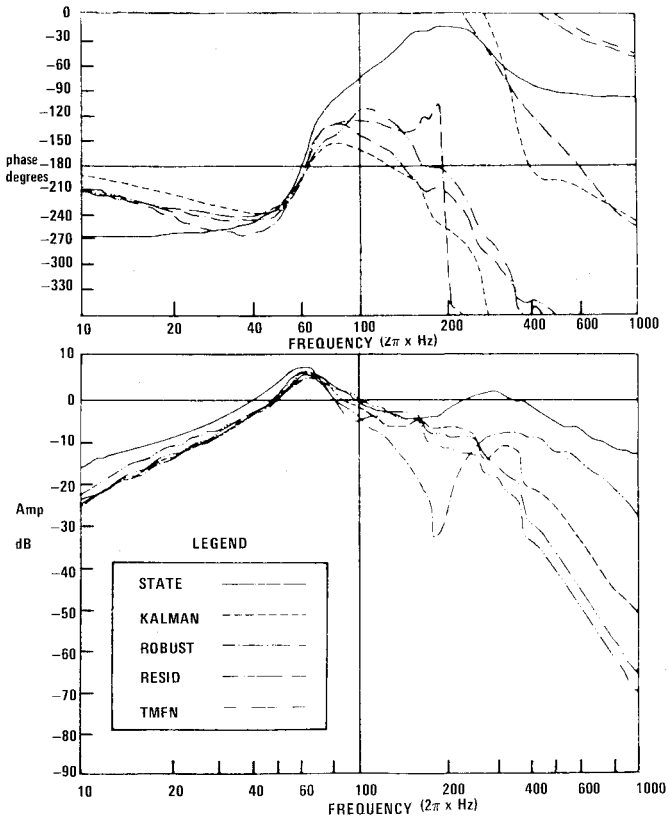

Fig. 3 Bode plots of transfer function from actuator input to feedback compensator output for a single sensor at 4 (2T).

in minimum phase transfer functions. As the value of the design parameter b increases both robustness and rms response increase. The value of $b=0.000001$ for the robustness parameter provides a good compromise between rms response and robustness. This value is used for subsequent robust estimator designs.

Final Sensor Placement

Based on the results obtained above, additional sensor locations are examined in order to improve system performance when implemented with a robust Kalman estimator. Single sensor and double sensor cases are considered.

Single Sensor

Sensors are placed at eight positions along the trailing edge spar and two positions on the leading edge of the spar and transfer zeroes computed. The three node positions (16, 19, and 22) on the trailing edge of the spar centered about the aileron result in minimum phase transfer functions. The performance results of full-state feedback control are tabulated in row 1 of Table 4. Robust Kalman estimators (with $b=0.000001$) are synthesized with the sensor at node points 16, 19, and 22, and the system performance is listed in rows 3-5 of Table 4. Node point 16 is better than node point 19 which is better than node point 22. The gain margins are good, but the phase margins need to be increased 15 to 20 deg. The rms control surface deflection exceeds the limit of 4 deg but deflection rates are below the limit of 250 deg/s. Increasing the robustness parameter would increase the phase margins at the expense of rms surface activity and vice versa. So, improved performance is sought by moving the sensor. Since the positions on the trailing edge of the spar are exhausted, sensors are positioned aft of the spar. The notation 19 (2T) indicated the point twice as far from the elastic axis as the node point 19 (see Fig. 1). Additional locations 16 (2T), 4 (2T), 4 (3T), 13(2T), 10 (2T), and 7 (2T) are also examined.

Rows 6-12 of Table 4 present the results. Moving aft and toward the tip improved performance. Although 4 (3T) has better performance than 4 (2T), 4 (2T) is selected because of concern about accessibility of 4 (3T). Using the accelerometer at 4 (2T), gain margins are excellent (-14.6 dB and $+6.5$ dB) but phase margins (± 52.7 deg) should be increased by 7.3 deg. The control surface deflection and rate meet the design specifications.

A comparison (rows 2 and 11) of the results with the Kalman estimator and robust estimator for node point 4 (2T) shows robustness costs 8 and 13% in deflection and rate. Gain margins changed from -3.7 dB and $+7.3$ dB to -14.6 dB and $+6.5$ dB; phase margins changed from -65.4 deg and $+31.9$ deg to ± 52.7 deg (see Fig. 3). Using accelerometer positions 22 and 4 (2T) as extremes illustrates the benefits achieved by searching for better sensor positions. Rms response for δ was improved by 14% and $\dot{\delta}$ by 7%. Improvements of 1 dB in positive gain margin, 9 deg in negative phase margin, and 5 deg in positive phase margin resulted.

Double Sensors

The search for the best sensor position is made in the same way for the double sensor case as for the single sensor case. Table 5 presents the results. The first row contains the results for full-state feedback. Kalman and robust estimator data with sensors at nodes 2 and 6 are presented in rows 2 and 3. These are considered to be the best positions for sensors restricted to the leading and trailing edge of the spar. The rms deflection of 3.008 is considerably less than the limit of 4 deg and the rms deflection rate of 224.4 is slightly smaller than the limit of 250 deg/s. The gain margins and bandwidth are good. Rows 4 through 9 show results for other sensor positions on the spar. Stability margins and bandwidth are almost totally unaffected as sensor placement changes. However, the rms

Table 5 Double sensor robust controller performance

Control	Sensor node position	Rms δ, deg	Rms $\dot{\delta}$, deg/s	Rms J ($\times 10^7$)
State	...	2.579	189.4	.05529
Kalman	2,6	3.033	203.6	.07501
Robust	2,6	3.008	224.4	.1051
Robust	40,42	3.748	264.0	.1325
Robust	4,6	3.200	222.9	.1062
Robust	4,12	3.177	223.4	.1053
Robust	16,33	3.263	241.4	.1111
Robust	10,30	3.216	232.6	.1090
Robust	19,48	3.289	243.5	.1119
Robust	4 (2T),6 (2T)	2.984	214.2	.09904

deflection and rate are improved by 10 and 15% by optimization of the sensor location. As for the single sensor placement, sensors were also moved aft of the spar. The results are presented in row 10 where the sensors are placed twice as far from the elastic axis as node 4. Only a small improvement was obtained.

V. Practical Flutter Controllers

The robust Kalman estimator together with the optimal state feedback gains constitute an optimal controller which can be implemented. However, the cost of implementation can be significantly reduced by developing low-order approximations to the optimal controller. These low-order approximations must 1) achieve closed loop asymptotic stability; 2) maintain ample gain and phase margins; 3) maintain low bandwidth; and 4) maintain acceptable rms responses.

Two methods are used to develop practical flutter controllers. These are modal residualization[20] and frequency response matching.[19] In residualization, the optimal controller is split into two parts. In the first part (low-frequency portion) the dynamics are retained. In the second part (high-frequency portion) only steady-state terms are retained. In frequency response matching, the transfer function between the measurement and control is approximated by a low-order transfer function. The order of the approximating transfer function is first assumed and then the coefficients are obtained to provide a best least-squares fit to the actual transfer function over a range of frequencies.

The optimal flutter controller, consisting of the robust Kalman estimator and the full-state feedback gains, is simplified to obtain three practical flutter controllers. Two of them use a single sensor at node point 4 ($2T$). The first approximates the optimal flutter controller by residualization and the second approximates it by frequency response matching. The third employs two sensors at node points 2 and 6 and is obtained by modal residualization. All controllers meet the rms requirements and exhibit reasonably good stability margins.

Table 6 presents the performance results for the single sensors. Rows 1, 2, and 3 show the state, Kalman and robust results discussed previously. Rows 4 and 5 summarize results with the best residualized controller. This controller is obtained by retaining the first two flexure modes in the estimator, by deleting a small direct transfer term and by adding a first-order lag with a 1/300 s time constant to meet roll-off requirements. In row 4 the sensor measurement noise is set to zero. A comparison of rows 3 and 5 show that residualization reduced the rms activity. The rms deflection of 3.41 deg and rate of 184.3 deg/s are well below the limit of 4 deg and 250 deg/s. The adverse effect of residualization is in stability margin reduction. The gain margins of -5.0 and $+5.5$ are below the objective of $+6.0$ dB. The phase margin is also reduced to about 40 deg and the bandwidth is increased from 17 to 25.6 Hz.

Table 6 Single sensor practical controller performance

Control	Sensor node position	Rms δ, deg	Rms $\dot{\delta}$, deg/s
State	...	2.58	189.4
Kalman	4 ($2T$)	3.33	186.6
Robust	4 ($2T$)	3.59	209.7
Resid[a]	4 ($2T$)	3.16	180.3
Resid	4 ($2T$)	3.41	184.3
Trnfn[a]	4 ($2T$)	3.23	184.3
Trnfn	4 ($2T$)	3.42	189.3

[a] Without sensor measurement noise.

Table 7 Double sensor practical controller performance

Control	Sensor node position	Rms δ, deg	Rms $\dot{\delta}$, deg/s
State	...	2.58	189.4
Kalman	2,6	3.03	203.6
Robust	2,6	3.01	224.4
Resid[a]	2,6	3.04	197.6
Resid	2,6	3.27	215.3

[a] Without sensor measurement noise.

Similar results are obtained with frequency response matching using a second-order-numerator/third-order-denominator approximation. The rms values and gain margins are good, but another 4 deg in positive phase margin is lost. Figure 3 presents the Bode plots for the transfer functions from the actuator input to the output of the feedback compensator for the full-state, Kalman, robust Kalman, residualized, and frequency response matching cases. The figure shows that achieving the desired rms response at the full-state feedback design level forces excessive bandwidth on the system. Both practical controllers achieve good roll off after 23.9 Hz.

Table 7 presents the performance summary for the double sensor practicalization results. Rows 1, 2, and 3 are for full-state control and control with Kalman and robust Kalman estimators. Rows 4 and 5 are results from using the best controller obtained by retaining the first two flexure modes and the gust model states in the estimator during the residualization; a small direct transfer term is dropped and the roll-off filter added. The effect of residualization is a small but acceptable increase in rms control surface deflection and a decrease in rate. Phase margins are improved and are acceptable. Most serious is the loss in positive gain margin. Figure 4 compares the frequency responses of the transfer functions from the actuator input to feedback compensator

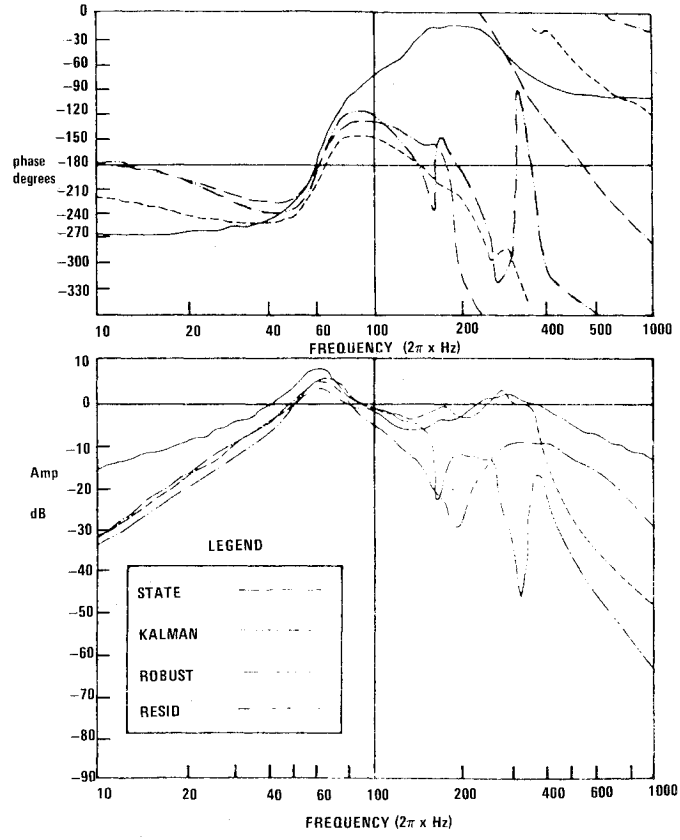

Fig. 4 Bode plots of transfer function from actuator input to feedback compensator output for two sensors at 2 and 6.

output for the full-state, Kalman, robust Kalman, and residualized controllers. The Kalman controller attempts to maintain the high bandwidth of the full-state control. The bandwidth of the robust Kalman controller is much smaller than that for the Kalman controller. The residualized practical controller is quite similar to the robust Kalman controller.

Transfer functions between the accelerometer output and actuator input for the three final practical controllers are presented in Table 8. The two single sensor controllers look good. They are stable and minimum phase. Poles and zeros are neither excessively large nor small. The double sensor controller (obtained by residualization) is nonminimum phase but is otherwise satisfactory.

VI. Performance Analysis

The residualized practical controller with a single accelerometer located at point 4 ($2T$) is selected for final evaluation. The performance of the control system is evaluated using more accurate flutter models than the one used in developing the design in order to assess the sensitivity of calculated performance to model accuracy. The rms values of control surface displacement and velocity increase with the number of aerodynamic lag terms and flexure modes included in the model. The gain and phase margins remain about the same for all models and the bandwidth increases only when the most accurate model is used (eight flexure modes and four aerodynamic lag terms at $\hat{k}=0.2$, 0.4, 0.6, and 0.8). None of these increases are large and it appears that the design flutter model using five flexure modes and one aerodynamic lag term at $\hat{k}=0.2$ is sufficiently accurate. Figure 2 presents the root locus as dynamic pressure is varied at Mach 0.9 for the eight flexure modes with and without a flutter controller (four aerodynamic lag terms are used in the model). Only the lowest two models are affected substantially by the presence of the flutter controller. All subsequent evaluations are performed using a flutter model with five flexure modes and four aerodynamic lag terms.

At the design Mach number of 0.9 and dynamic pressure of 7.66 kPa the performance of the residualized design with no sensor noise compares favorably with that of designs based on the aerodynamic energy approach and linear optimal control theory.[7] The aerodynamic energy method results in a flutter dynamic pressure of 10.44 kPa (218 psf). At 7.25 kPa (151 psf) the rms control surface deflection is 3.6 deg and the rms deflection rate is 187 deg/s. Linear optimal control results in a flutter dynamic pressure of 9.03 kPa (188.6 psf) and rms control surface displacement of 4.1 deg and rms deflection rate of 218 deg/s at 7.24 kPa. The residualized controller results in a flutter dynamic pressure of 10.39 kPa (217 psf) and rms control surface deflection of 3.65 deg and rms deflection rate of 204.2 deg/s at 7.66 kPa. Gain and phase margins for this controller are comparable with those obtained by the use of the aerodynamic energy method and linear-optimal control.[7]

The performance of the residualized design was evaluated over a range of dynamic pressures for Mach numbers of 0.9, 0.8, and 0.7. The results are presented in Table 9 and Fig. 5. An increase in flutter dynamic pressure of 44% is achieved at all Mach numbers. For a given Mach number, the rms control surface displacement, rms control surface rate, and bandwidth increase with dynamic pressure. In terms of stability, the worst gain margin is 2.91 dB and the worst phase margin is 14.81 deg (note that both of these are at dynamic pressure

Table 8 Practical controller transfer functions

Method	Sensor	Transfer functions
Resid	4 ($2T$)	$(0.003987)\dfrac{(300)(s^2+2*0.6600*88.43s+88.43^2)(s+22.91)}{(s+300)(s^2+2*0.6921*53.19*s+53.19^2)(s^2+2*0.7379*19.03*s+19.03^2)}$
Trnfn	4 ($2T$)	$(0.006855)\dfrac{(300)(s^2+2*0.1496*92.57*s+92.57^2)}{(s+300)(s^2+2*0.4247*70.04*s+70.04^2)(s+17.65)}$
Resid	2	$(0.009367)\dfrac{(300)(s^2+2*0.6258*18.57*s+18.57^2)(s^2+2*0.9991*4.477*s+4.477^2)(s+158)}{(s+300)(s^2+2*0.6818*26.73*s+26.73^2)(s^2+2*0.9938*7.498*s+498^2)(s+154.9)(s+3.973)}$
	6	$(-0.010467)\dfrac{(300)(s^2+2*0.9989*4.488*s+4.488^2)(s-20.64)(s+97.06)(s+20.01)}{(s+300)(s^2+2*0.6818*26.73*s+26.73^2)(s^2+2*0.9938*7.498*s+7.498^2)(s+154.9)(s+3.973)}$

Table 9 Performance variation with Mach number and dynamic pressure for the DAST half wing

Mach number	Dynamic pressure $\bar{q}$, kPa	Control surface deflection (rms), deg	Control surface velocity (rms), deg/s	Gain margin				Phase margin				Bandwidth, Hz
				dB	Hz	dB	Hz	deg	Hz	deg	Hz	
0.7	3.83	1.79	84.63	−13.47	23.83	...	...	−104.5	4.19	27.27	9.36	17.7
	5.75	2.88	173.38	−10.07	23.83	...	...	−112.76	4.76	27.12	10.57	18.5
	7.66	4.44	284.88	−7.68	23.61	3.03	10.92	−103.5	8.67	34.32	14.30	20.2
	9.58	4.80	279.54	−5.83	23.77	2.91	10.84	−23.84	9.02	22.39	14.98	24.5
0.8	3.83	1.88	90.18	−12.54	23.81	...	...	−104.62	4.25	25.60	9.34	18.3
	5.75	3.02	177.96	−9.15	23.84	19.19	8.88	−113.89	5.02	29.54	10.38	19.4
	7.66	4.05	240.81	−6.78	23.84	3.95	10.42	−73.80	8.64	37.08	15.01	21.6
	9.58	4.95	257.55	−4.95	23.83	4.16	10.29	−22.38	8.09	25.48	15.93	25.6
0.9	3.83	2.03	97.93	−11.17	23.62	...	...	−105.38	4.37	24.32	9.27	18.8
	5.75	3.09	173.15	−7.85	23.77	13.41	9.03	−114.27	5.48	37.88	10.15	20.7
	7.66	3.85	207.70	−5.48	23.82	5.21	9.84	−55.36	8.11	36.70	16.23	25.6
	9.58	6.07	274.91	−3.65	23.84	5.68	9.69	−14.81	7.06	25.84	17.44	27.1

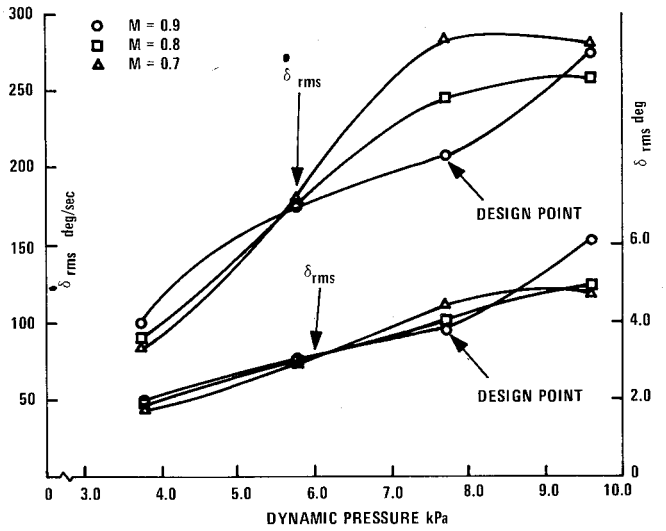

Fig. 5 Performance of the final flutter controller.

Table 10 Flutter dynamic pressure and flutter frequency variation with Mach number

Mach number	Without flutter suppression control		With flutter suppression control	
	$\bar{q}_f$, kPa	f_f, Hz	$\bar{q}_f$, kPa	f_f, Hz
0.7	6.32	9.266	11.72	6.871
0.8	5.75	8.650	11.08	6.584
0.9	4.96	8.029	10.39	6.272

of 9.58 kPa or 200 psf). If the dynamic pressure is less than 7.66 kPa (the design value), the worst gain margin is 3.03 dB and the worst phase margin is 25.6 deg. For a Mach number of 0.7 the limits on both control surface deflection and rate are exceeded at the design dynamic pressure of 7.66 kPa.

The rms values obtained with the residualized controller for off-design Mach numbers and dynamic pressures are higher than those reported for the controller designed using the aerodynamic energy approach and are comparable to those reported for the linear-optimal controller.[7] However, a direct comparison of the results presented in Fig. 5 with those in Ref. 7 is somewhat misleading. The evaluation of the controllers described in Ref. 7 did not include sensor noise, whereas the residualized controller described in this paper includes sensor noise. Also structural damping was neglected in the performance evaluation of the residualized controller but was included in the evaluation of the controllers designed using the aerodynamic energy approach and linear optimal control theory. The addition of structural damping would probably improve the performance of the residualized design.

VII. Conclusions

Linear quadratic Gaussian (LQG) design methodology can be usefully applied to the synthesis of active flutter control systems provided adequate gain and phase margins are maintained. Conventional Kalman estimators result in gain and phase margins which are unacceptably small; however, the Doyle-Stein procedure for robust estimator design, coupled with proper choice of sensor locations, can be used to improve these margins to acceptable values without causing excessive control surface activity. Both modal residualization and frequency response matching techniques can be used to obtain reduced-order approximations of the control system design resulting from the robust LQG theory. Both of these methods yield controllers which satisfy performance specifications over a range of dynamic pressures at the design Mach number; however, as the Mach number is decreased, control surface activity increases and actual implementation may require gain scheduling with Mach number.

Acknowledgments

This work was performed under NASA Contract No. NAS 1-15486.

References

[1]Shomber, A., "Application of Integrated Active Controls to Future Transports," AIAA Paper 79-1654, *Proceedings of 1979 Guidance and Control Conference,* Aug. 1979.

[2]Murrow, H.N. and Eckstrom, C.V., "Drones for Aerodynamic and Structural Testing (DAST) – A Status Report," AIAA Paper 78-1485, 1978 Atmospheric Flight Mechanics Conference, Aug. 1978.

[3]Abel, P.B. III and Murrow, H.N., "Two Synthesis Techniques Applied to Flutter Suppression on a Flight Research Wing," *Journal of Guidance and Control,* Vol. 1, Sept.-Oct. 1978, pp. 340-346.

[4]Visor, O.E. and Sevart, F.D., "Preliminary Design Study of Flutter Suppression for BQM-34/F Drone Aircraft with a Supercritical Wing – Final Report," NASA CR-145208, 1976.

[5]Nissim, E., "Comparative Study Between Two Different Active Flutter Suppression Systems," *Journal of Aircraft,* Vol. 15, Dec. 1978, pp. 843-848.

[6]Newsom, J.R., "Control Law Synthesis for Active Flutter Suppression Using Optimal Control Theory," *Journal of Guidance and Control,* Vol. 2, Sept.-Oct. 1979, pp. 388-394.

[7]Abel, I., Newsom, J.R., and Dunn, H.J., "Application of Two Synthesis Methods for Active Flutter Suppression of an Aero-Elastic Wind Tunnel Model," AIAA Paper 79-1633, 1979 Atmospheric Flight Mechanics Conference, Aug. 1979.

[8]Johnson, T.L., Athans, M., and Skelton, G.B., "Optimal Control Surface Location for Flexible Aircraft," *IEEE Transactions on Automatic Control,* Vol. AC-16, Aug. 1971, pp. 320-331.

[9]Doyle, J.C. and Stein, G., "Robustness with Observers," *IEEE Transactions on Automatic Control,* Vol. 24, Aug. 1979, pp. 607-610.

[10]Albano, E. and Rodden, W.P., "A Doublet Lattice Method for Calculating Lift Distributions on Oscillating Surfaces in Subsonic Flows," *AIAA Journal,* Vol. 7, Feb. 1969, pp. 279-289.

[11]Sevart, F.D., "Development of Active Flutter Suppression Wind Tunnel Testing Technology," AFFDL-TR-74-126, 1975.

[12]Jones, R.T., "The Unsteady Lift of a Wing of Finite Aspect Ratio," NACA Rept. 681, 1940.

[13]Edwards, J.W., Breakwell, J.V., and Bryson, A.E. Jr., "Active Flutter Control Using Generalized Unsteady Aerodynamic Theory," *Journal of Guidance and Control,* Vol. 1, Jan.-Feb. 1978, pp. 32-40.

[14]Vepa, R., "Finite State Modeling of Aeroelastic Systems," NASA Contractor Report CR-2779, Feb. 1977.

[15]Weiss, S.J., Tseng, K., and Morino, L., "State-Space Formulation for Flutter Analysis," AIAA Paper 77-117, 1977 Aerospace Sciences Meeting, 1977.

[16]Abel, I., "An Analytical Technique for Predicting the Characteristics of a Flexible Wing Equipped with an Active Flutter Suppression System and Comparison with Wind Tunnel Data," NASA TP-1367, Feb. 1979.

[17]Kwakernaak, H. and Sivan, R., *Linear Optimal Control Systems,* John Wiley and Sons, New York, 1972, pp. 281-311.

[18]Sirisena, H.R., "Optimal Control of Saturating Linear Plants for Quadratic Performance Indices," *International Journal of Control,* Vol. 8, June 1968, pp. 65-87.

[19]Mahesh, J.K., Stone, C.R., Garrard, W.L., and Hausman, P.D., "Active Flutter Control for Flexible Vehicles," NASA Contractor Rept. 159160, Nov. 1979.

[20]Harvey, C.A. and Pope, R.E., "Study of Synthesis Techniques for Insensitive Aircraft Control Systems," NASA CR2803, April 1977.

[21]Brown, R.G., "Linear State Space Analysis," Ph.D. Thesis, Iowa State University, Ames, Iowa, June 1967.